Journal of
Composites Science

MDPI

Article

Nanostructured K- and Na-Substituted Aluminosilicates for Ni(II) Ions Removal from Liquid Media: Assessment of Sorption Performance and Mechanism

Ekaterina Nekhludova [1,2], Nikita Ivanov [3,4], Sofia Yarusova [1,2], Oleg Shichalin [3,4,*], Yulia Parotkina [5], Alexander Karabtsov [6], Vitaly Mayorov [6], Natalya Ivanenko [2], Kirill Barkhudarov [3,6], Viktoriya Provatorova [3], Viktoriya Rinchinova [3], Vladimir Afonchenko [3], Sergei Savin [7], Vasilii Ivanovich Nemtinov [3], Anton Shurygin [3], Pavel Gordienko [1] and Eugeniy Papynov [3]

1 Laboratory of Protective Coatings and Marine Corrosion, Institute of Chemistry, Far Eastern Branch of Russian Academy of Sciences, 159 Prosp. 100-Letiya Vladivostoka, Vladivostok 690022, Russia; astapovnna@bk.ru (E.N.); yarusova_10@mail.ru (S.Y.); pavel.gordienko@mail.ru (P.G.)
2 The Basic Department of Ecology and Ecological Problems of Chemical Technology, Vladivostok State University, Gogolya st., 41, Vladivostok 690014, Russia; ivanenko_natalya@mail.ru
3 Institute of High Technologies and Advanced Materials, Far Eastern Federal University, 10 Ajax Bay, Russky Island, Vladivostok 690922, Russia; ivanov.np@dvfu.ru (N.I.); barkhudarov.kv@dvfu.ru (K.B.); provatorova.vv@dvfu.ru (V.P.); rinchinova.vb@dvfu.ru (V.R.); afonchenko.va@dvfu.ru (V.A.); nemtinov.vi@dvfu.ru (V.I.N.); shurygin.av@dvfu.ru (A.S.); papynov@mail.ru (E.P.)
4 Laboratory of Electrochemical Power Sources for Renewable Energy, Sakhalin State University, Communist Ave., 33, Yuzhno-Sakhalinsk 693008, Russia
5 Laboratory of Molecular and Elemental Analysis, Institute of Chemistry, Far Eastern Branch of Russian Academy of Sciences, 159 Prosp. 100-Letiya Vladivostoka, Vladivostok 690022, Russia; azarova.87@mail.ru
6 Laboratory of X-Ray Methods, Far East Geological Institute, Far Eastern Branch of Russian Academy of Sciences, 159 Prosp. 100-Letiya Vladivostoka, Vladivostok 690022, Russia; karabzov@fegi.ru (A.K.); 024205@inbox.ru (V.M.)
7 Department of Synchrotron Experimental Stations, National Research Centre "Kurchatov Institute", Akademika Kurchatova pl. 1, Moscow 123182, Russia; bellaccqua@gmail.com
* Correspondence: oleg_shich@mail.ru

check for updates

Academic Editor: Giuseppe Cavallaro

Received: 4 August 2025
Revised: 4 September 2025
Accepted: 10 September 2025
Published: 1 October 2025

Citation: Nekhludova, E.; Ivanov, N.; Yarusova, S.; Shichalin, O.; Parotkina, Y.; Karabtsov, A.; Mayorov, V.; Ivanenko, N.; Barkhudarov, K.; Provatorova, V.; et al. Nanostructured K- and Na-Substituted Aluminosilicates for Ni(II) Ions Removal from Liquid Media: Assessment of Sorption Performance and Mechanism. *J. Compos. Sci.* **2025**, *9*, 530. https://doi.org/10.3390/jcs9100530

Abstract

The removal of nickel from industrial wastewater necessitates efficient sorbent materials. This study investigates nanostructured potassium- and sodium-substituted aluminosilicate-based nanocomposites for this application. Materials were synthesized and characterized using SEM-EDS, XPS, XRD, FTIR, low temperature N_2 adsorption–desorption and Ni^{2+} adsorption experiments. SEM and XRD confirmed an X-ray amorphous structure attributable to fine crystallite size. The sodium-substituted material $Na_2Al_2Si_2O_8$ exhibited the lowest specific surface area (48.3 m^2/g) among the tested composites. However, it demonstrated the highest Ni(II) sorption capacity (64.6 mg/g, 1.1 mmol/g) and the most favorable sorption kinetics, as indicated by a Morris-Weber coefficient of 0.067 ± 0.008 mmol/(g·min$^{1}/^{2}$). Potassium-substituted analogs with higher Si/Al ratios showed increased surface area but reduced capacity. Analysis by XPS and SEM-EDS established that Ni(II) uptake occurs through a complex mechanism, involving ion exchange, surface complexation, and chemisorption resulting in the formation of new nickel-containing composite surface phases. The results indicate that optimal sorption performance for Ni(II) is achieved with sodium-based aluminosilicates at a low Si/Al ratio (Si/Al = 1). The functional characteristics of $Na_2Al_2Si_2O_8$ compare favorably with other silicate-based sorbents, suggesting its potential utility for wastewater treatment. Further investigation is needed to elucidate the precise local coordination environment of the adsorbed nickel.

Keywords: adsorption; nickel; aluminosilicate; sorption kinetics; sorption mechanism

1. Introduction

Nickel and its compounds are extensively used across various industrial sectors, including chemical manufacturing, electroplating, and pharmaceutical production. Due to their high toxicity, contamination by nickel and its compounds poses a significant environmental concern [1]. Anthropogenic activities substantially contribute to the accumulation of Ni in soils and water bodies, increasing the risk of its introduction into terrestrial ecosystems and food production systems. This poses a threat not only to food security but also to human health and environmental integrity [2–5]. Due to the high toxicity of nickel, the World Health Organization has established guidelines stipulating that nickel concentration in drinking water should not exceed 0.07 mg/L (70 μg/L) [6].

Adsorption technology for nickel removal from wastewater offers several significant advantages over alternative treatment methods: (1) high removal efficiency even at low concentrations of contaminants; (2) relatively simple process design and operation without requirements for complex equipment; (3) high selectivity toward nickel ions with appropriate adsorbent selection; (4) regeneration capability and reusability of adsorbents with potential nickel recovery from regeneration solutions; (5) environmental compatibility through elimination of toxic reagents and prevention of secondary pollution; (6) operational flexibility and adaptability to varying conditions [7–9].

In this context, extensive research is being conducted to identify sorbents for nickel ion removal from aqueous solutions, with natural and synthetic aluminosilicates, along with their derived materials, representing a particularly significant group [10–13]. Aluminosilicates have emerged as promising heavy metal sorbents due to their cost-effectiveness, diversity, and natural abundance.

A comprehensive review [14], examining the structure, properties, and characteristics of aluminosilicates in terms of their sorption applications highlights that aluminosilicate-based materials serve as effective heavy metal sorbents owing to their high affinity, selectivity, reactivity, and substantial specific surface area. However, it is noted that in certain cases, aluminosilicates may exhibit lower sorption properties compared to synthetic adsorbents. Consequently, their properties are often enhanced through functionalization processes, including thermal activation, acid activation, and intercalation, among others.

The sorption capacity of various aluminosilicates (bentonite, palygorskite, vermiculite, montmorillonite, kaolinite, muscovite, etc.) towards Ni^{2+} ions ranges from 0.8 to 124.3 mg/g. Notably, a remarkably high nickel ion sorption capacity (up to 1227.2 mg/g) has been reported for a geopolymer based on bentonite clay modified with Fe_3O_4 nanoparticles [15]. Modification of aluminosilicates with phosphates allowed achieving high sorption capacity of 193.98 mg/g for Ni^{2+} and 185.78 mg/g for Cd^{2+} [16].

A novel synthesis method for mesoporous aluminosilicate composite using glass waste from thin-film transistor liquid crystal displays was proposed in [17]. The composite, with a specific surface area of 175 $m^2 \cdot g^{-1}$, demonstrated high efficiency as a heavy metal ion adsorbent. The maximum sorption capacity for Ni^{2+} ions reached 23.1 mg/g at pH 3.5. Furthermore, the composite's environmental applicability was evaluated through column experiments using actual electroplating wastewater. These experiments confirmed the composite's ability to effectively remove Ni^{2+} from electroplating wastewater with a sorption capacity of 18.7 mg/g.

Our previous research focused on investigating the sorption properties of nanocomposite aluminosilicates with varying Si/Al ratios, represented by the formula $M_2Al_2Si_xO_{(2x+4)}$.

nH_2O (where M = K^+, Na^+; x = 2, 10), including their modified forms [18–20]. These compounds, synthesized from aqueous multicomponent systems, demonstrated high sorption capacities towards cesium ions. Investigation of both potassium and sodium is important because these cations influence the porous structure development and impact the kinetic parameters of the adsorption process.

The present study aims to investigate the sorption capacity and kinetic characteristics, as well as to elucidate the mechanism of nickel ion adsorption on nanostructured potassium and sodium aluminosilicates with varying Si/Al ratios ($M_2Al_2Si_xO_{(2x+4)}.nH_2O$, where M = K^+, Na^+; x = 2, 10). This investigation will assess these materials' potential as highly effective heavy metal sorbents.

The scientific novelty of the research lies in the use of X-ray amorphous nanostructured aluminosilicates with variable Si/Al ratio as sorbents for Ni^{2+} removal. Additionally, the fundamental mechanisms of nickel ion interaction with the surface of X-ray amorphous silicate materials $M_2Al_2Si_xO_{(2x+4)}\cdot nH_2O$ have been investigated using SEM-EDS microscopy, XPS, and physicochemical methods for studying adsorption processes. The formation of nanocomposite of nickel-containing phases and initial amorphous aluminosilicate during the sorption of nickel from liquid media was demonstrated.

2. Materials and Methods

The synthesis methodology for potassium and sodium aluminosilicates with specified Si/Al ratios has been previously described in our works [18–20].

Sorption properties were investigated in batch experiments at 20 °C with a solid-to-liquid ratio of 1:100 using aqueous solutions of nickel chloride ($NiCl_2\cdot 6H_2O$) with initial Ni^{2+} ion concentrations ranging from 0.83 to 18.41 mmol·L^{-1}. Adsorption kinetics were studied under similar conditions at 20, 40, and 70 °C using aqueous solutions with Ni^{2+} ion concentrations of 8.45–9.8 mmol·L^{-1}. The contact times were 0.05, 0.117, 0.25, and 0.5 h. All adsorption tests were performed in duplicate experiments.

Model wastewater containing lead, nickel, manganese, and copper was prepared from stock solutions, with precise metal concentrations determined by atomic absorption spectrometry (AAS). Groundwater samples were collected at Berendey Waterfall (Partizansky Urban District, Primorsky Krai, Russia). Seawater samples were collected from Ajax Bay (Russky Island, Vladivostok Urban District, Primorsky Krai, Russia). The exact ion concentrations in the groundwater samples were determined by AAS. Nickel solution was added to the original groundwater and seawater samples to achieve an initial Ni concentration approaching 20 mg/L.

Ni^{2+} ion concentrations in initial solutions and post-sorption filtrates were determined by AAS using a Solaar M6 double-beam spectrometer (Thermo Scientific, Waltham, MA, USA) at wavelength of 232 nm. The detection limit for nickel ions in aqueous solutions was 0.05 μg/mL.

The experimental adsorption data were analyzed using well-established models: Langmuir, Freundlich, and Langmuir-Freundlich isotherms [21] for equilibrium studies, and pseudo-first-order, pseudo-second-order, and intraparticle diffusion models [22] for kinetic studies.

Structural characterization of pristine and saturated materials was performed using a D8 ADVANCE automatic diffractometer (Bruker, Karlsruhe, Germany) with sample rotation in CuKα radiation.

The thermogravimetric and differential thermal analysis (TG-DTA) curves were recorded on the DTG-60H Shimadzu device in platinum crucibles with a pierced lid in a dry argon stream (20 mL/min) in the temperature range of 35–1300 °C at the heating rate of 10 °C/min (Shimadzu, Kyoto, Japan).

Fourier transform infrared (FTIR) absorption spectra were recorded on a Fourier transform spectrophotometer "Iraffinity-1S" (Shimadzu, Kyoto, Japan).

Sample density was determined by pycnometry. Specific surface area, pore volume, and pore size distribution of sodium aluminosilicate samples were analyzed using low temperature nitrogen adsorption technique (−196 °C) on Autosorb-iQ surface area analyzer (Quantachrome, Boynton Beach, FL, USA). Sample preparation for porosity analysis included degassing at 100 °C using the integrated degassing station of the Autosorb-iQ analyzer.

Elemental composition of the synthesized aluminosilicates was quantified using energy-dispersive X-ray fluorescence spectroscopy on a EDX 800 HS spectrometer (Shimadzu, Kyoto, Japan).

XPS spectra were recorded using a spectrometer (SPECS, Berlin, Germany) equipped with a Phoibos 150 mm radius analyzer (SPECS, Berlin, Germany. AlKα radiation (1486.7 eV) served as the excitation source. Calibration was performed using an internal standard, with the C 1s peak of aliphatic and aromatic carbon set to 285.0 eV. All spectra were recorded at a constant analyzer pass energy of 50 eV. Survey spectra were collected with a 1 eV step, while detailed spectra of characteristic lines were recorded with a 0.1 eV step. Spectral processing was performed using CASA XPS Ver. 2.3.26PR1.0 software.

Surface morphology was examined by scanning electron microscopy (SEM) using ULTRA 55 Plus microscope (Carl Zeiss, Oberkochen, Germany) equipped with an X Max 80 energy-dispersive spectroscopy (EDS) detector (Oxford Instruments, Oxford, UK).

3. Results and Discussion

3.1. Characterization of Obtained Materials

To confirm the achievement of the target phase and elemental composition, as well as the nanostructured state of the obtained samples, XRD, FTIR, TGA-DTA, and SEM-EDS methods were employed (Figure 1). The diffractograms of the aluminosilicates (Figure 1a) exhibited a diffuse halo in the 2θ = 24–27° region, which is characteristic of X-ray amorphous silicate materials [23,24]. For the sodium-substituted samples, a shift of the halo toward lower 2θ angles was observed, indicating an increase in the interplanar spacing of these materials compared to the potassium-substituted samples. Such a characteristic X-ray amorphous diffraction pattern can be observed when the investigated material lacks long-range order or when the crystallite size is extremely small [25]. For our obtained materials, an extremely small crystallite size is characteristic while preserving long-range order in the crystal lattice [26]. This is confirmed by data from a series of complementary analytical methods for the condensed state of matter: SEM images indicate a nanostructured state of the material with individual crystallite sizes much smaller than 100 nm (Figure 2), FTIR spectra demonstrate characteristic absorption bands of crystalline aluminosilicates (Figure 1c), and TGA-DTA curves upon heating show mass loss without exothermic effects associated with crystallization (Figure 1d).

Figure 1b shows typical EDS maps of the distribution of main structural elements across the material surface using $Na_2Al_2Si_2O_8$ as an example. The uniform distribution of Al, Si, O, and Na(K) indicates the homogeneity of the phase composition of the obtained samples. To confirm the achievement of the target quantitative elemental composition, the content of main elements in the synthesized aluminosilicates was also evaluated by XRF (Table 1).

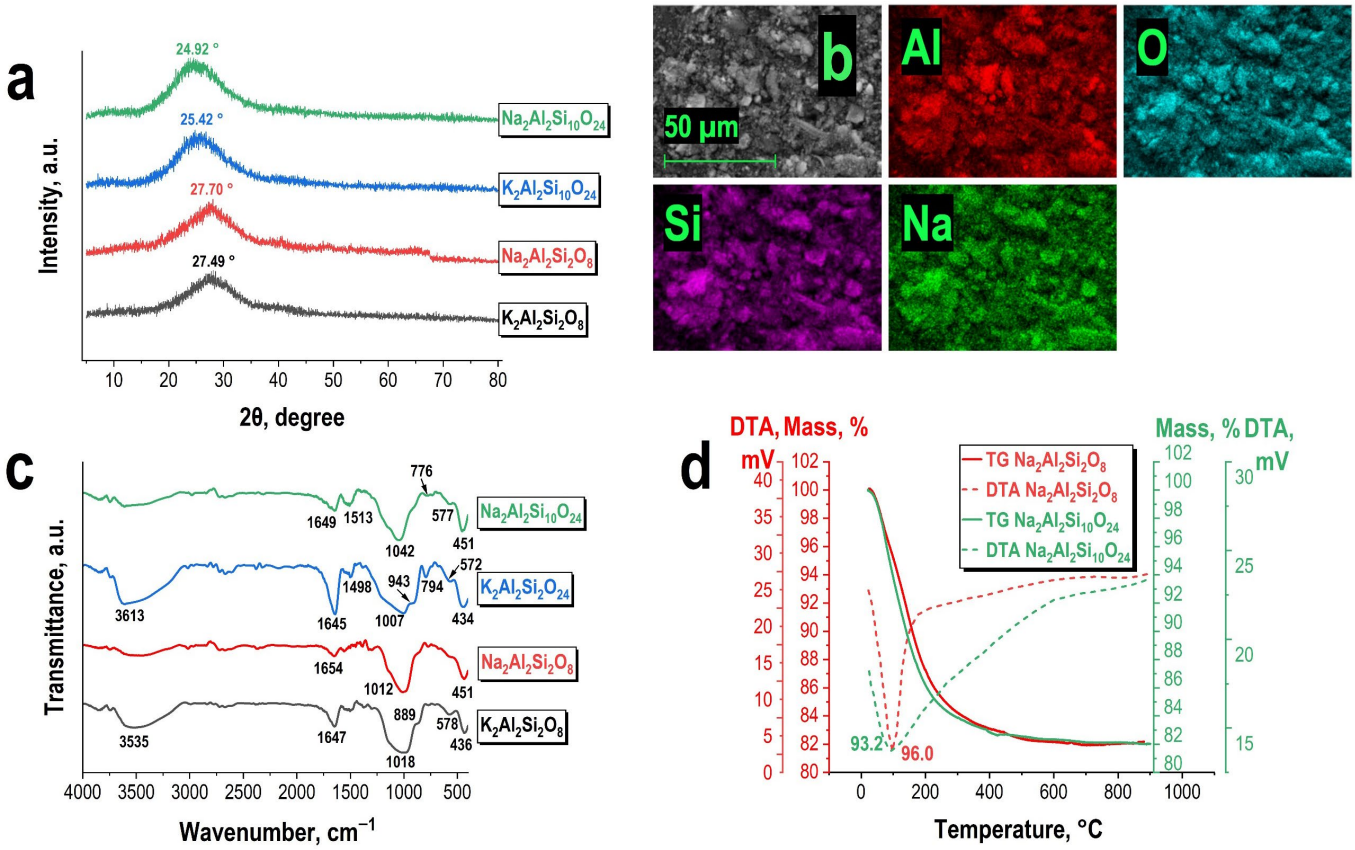

Figure 1. Physicochemical characterization of initial aluminosilicate materials: (**a**) XRD patterns, (**b**) EDS elemental distribution maps for $Na_2Al_2Si_2O_8$, (**c**) FTIR spectra, (**d**) TG-DTA curves.

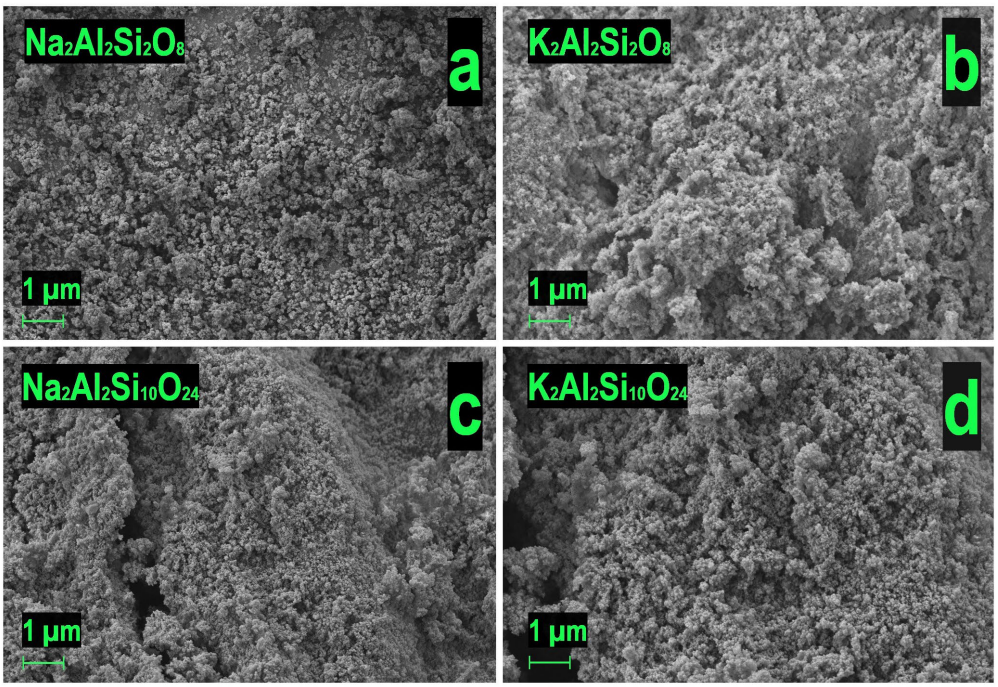

Figure 2. SEM-images of (**a**) $Na_2Al_2Si_2O_8$, (**b**) $K_2Al_2Si_2O_8$, (**c**) $Na_2Al_2Si_{10}O_{24}$, (**d**) $K_2Al_2Si_{10}O_{24}$.

Table 1. Elemental Composition and Textural Properties of obtained aluminosilicates as determined by XRF, Pycnometry and N^2 Adsorption.

Predicted Formula (Experimental Formula)	Nominal Si/Al Ratio (Experimental Si/Al Ratio)	Mass Content	Density, g/cm^3	S_{BET}, m^2/g
$K_2Al_2Si_2O_8$ ($K_{1.1}Al_2Si_{2.1}O_n$)	1.0 (1.04)	wt.%(K) = 27.20 wt.%(Al) = 35.10 wt.(Si) = 37.70	1.84	189.4
$K_2Al_2Si_{10}O_{24}$ ($K_{2.1}Al_2Si_{10.6}O_n$)	5.0 (5.3)	wt.%(K) = 18.64 wt.%(Al) = 12.53 wt.(Si) = 68.83	2.35	389.8
$Na_2Al_2Si_2O_8$ ($Na_{1.3}Al_2Si_{2.5}O_n$)	1.0 (1.2)	wt.%(Na) = 19.95 wt.%(Al) = 34.96 wt.(Si) = 45.09	1.54	48.3
$Na_2Al_2Si_{10}O_{24}$ ($Na_{1.4}Al_2Si_{9.4}O_n$)	5.0 (4.7)	wt.%(Na) = 9.20 wt.%(Al) = 15.42 wt.(Si) = 75.38	2.30	203.3

FTIR spectra (Figure 1c) are sufficiently informative for investigating the structure of X-ray amorphous aluminosilicates and contain a large number of characteristic absorption bands assigned to aluminosilicate materials according to available literature [27,28]: a broad band with a maximum in the 1042–1018 cm^{-1} region corresponds to asymmetric stretching vibrations of Si-O-Al bonds, the absorption band at 434–451 cm^{-1} is caused by vibrations of bridging Si-O-Si bonds, a shoulder in the 889–943 cm^{-1} region corresponds to vibrations of terminal Si-O bonds, and bands at 776–794 cm^{-1} and 572–578 cm^{-1} are attributed to deformation vibrations of the silicon-aluminum framework. Additionally, FTIR spectra of the initial samples contain absorption bands in the 3535–3613 cm^{-1} and 1645–1654 cm^{-1} regions, assigned to stretching and bending vibrations of water. For sodium-substituted samples, the characteristic water absorption bands exhibited higher intensity, indicating an increased degree of hydration of sodium-substituted aluminosilicates compared to potassium-substituted ones.

Based on the comparative analysis of SEM images (Figure 2), a reduction in particle and agglomerate size of $Na_2Al_2Si_{10}O_{24}$ (Si/Al = 5) compared to $Na_2Al_2Si_2O_8$ (Si/Al = 1) is evident. The aluminosilicate surface consists of numerous nanoscale spherical and quasi-spherical agglomerates. The diametrical dimensions of these particles are significantly below 100 nm (Figure 2), accounting for the X-ray amorphous nature of the sorbents. According to all obtained SEM-images, no significant morphological differences were observed between potassium- and sodium-substituted samples. These observed patterns align with our previously reported findings for a broader range of sodium-substituted aluminosilicates [20].

The mass loss observed on TG (Figure 1d) is explained by the removal of adsorbed and crystalline water, which is also confirmed by the presence of endothermic effects on the DTA curves. The absence of exothermic effects and other changes on the TG-DTA curves confirms the nanocrystalline structure of the material, since for a truly amorphous sample in the studied temperature range, crystallization processes would inevitably be observed [26].

The chemical composition of synthesized materials was evaluated using X-ray fluorescence analysis, with results presented in Table 1. The obtained Si/Al ratios in the materials match the theoretical values within experimental error. The specific surface area increased dramatically with increasing Si/Al ratio (Table 1), likely correlating with changes in average

particle size (Figure 2). Sodium- and potassium-substituted samples exhibited significantly different specific surface areas, suggesting potential variations in their sorption properties.

Low-temperature adsorption–desorption isotherms and DFT pore size distributions (Figure 3) allow detailed investigation of the differences in porous structure of the synthesized aluminosilicates. In terms of shape, the obtained isotherms belong to Type III according to IUPAC classification [29] and are characterized by the absence of a plateau at high P/P_0 values, indicating the presence of large macropores in the material structure. In the low relative pressure P/P_0 region, a characteristic plateau is present, indicating micropore filling. It should be noted that the micropore volume increases with increasing Si/Al ratio, which is explained by the decrease in material particle size (Figure 2). The hysteresis loops belong to H3-H4 type, indicating a slit-like pore shape between material particles. The pore size distributions constructed using the DFT method (Figure 3a*–d*) demonstrate significant differences between sodium-substituted and potassium-substituted materials. The $K_2Al_2Si_2O_8$ sample with Si/Al = 1 exhibited a polymodal pore size distribution with the largest contribution from mesopores with diameter d_p = 15 nm. As the Si/Al ratio increases to 5 for the $K_2Al_2Si_{10}O_{24}$ sample, the distribution character changes to monomodal with a dominant diameter of d_p = 8 nm. Sodium-substituted samples, in contrast, regardless of the ratio, possess a dominant mesopore diameter of d_p = 8–10 nm. For the sodium-substituted $Na_2Al_2Si_2O_8$ sample, an artifact in the micropore region (d_p = 4 nm) is also present on the DFT pore size distribution curve, the appearance of which is associated with the sharp closure of the hysteresis loop of the desorption branch (in accordance with [29]).

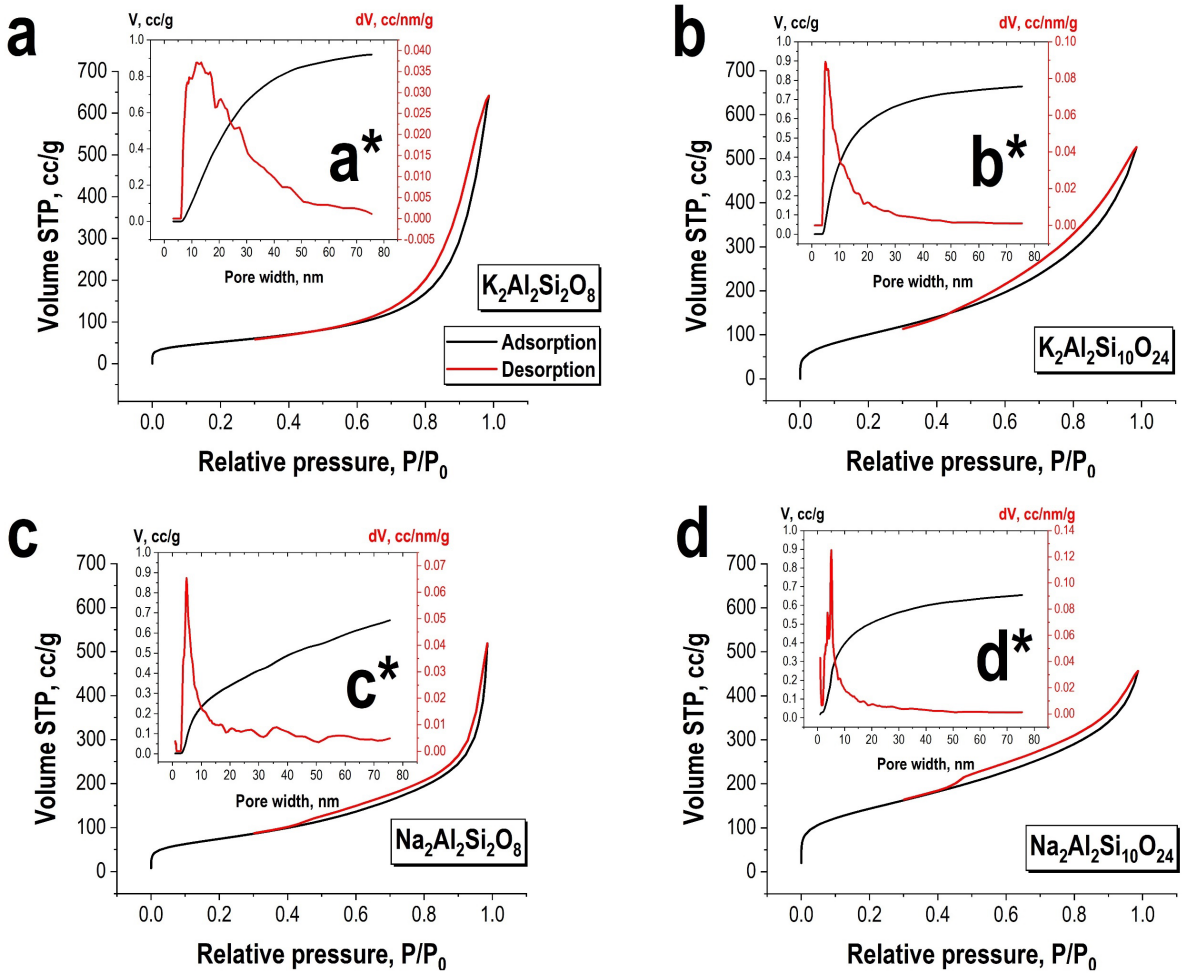

Figure 3. Isotherms of low-temperature N_2 adsorption–desorption (**a**–**d**) and DFT pore size distributions (**a***–**d***) for obtained aluminosilicate materials.

3.2. Sorption Perfomance Towards Ni^{2+} Ions

The sorption characteristics of the synthesized sorbents were evaluated using equilibrium adsorption method. Experimental adsorption isotherms for Ni^{2+} ions (Figure 4) were obtained during batch experiments in aqueous solutions without background electrolytes. The experimental data were analyzed using Langmuir, Freundlich, and Langmuir-Freundlich isotherm models (Table 2).

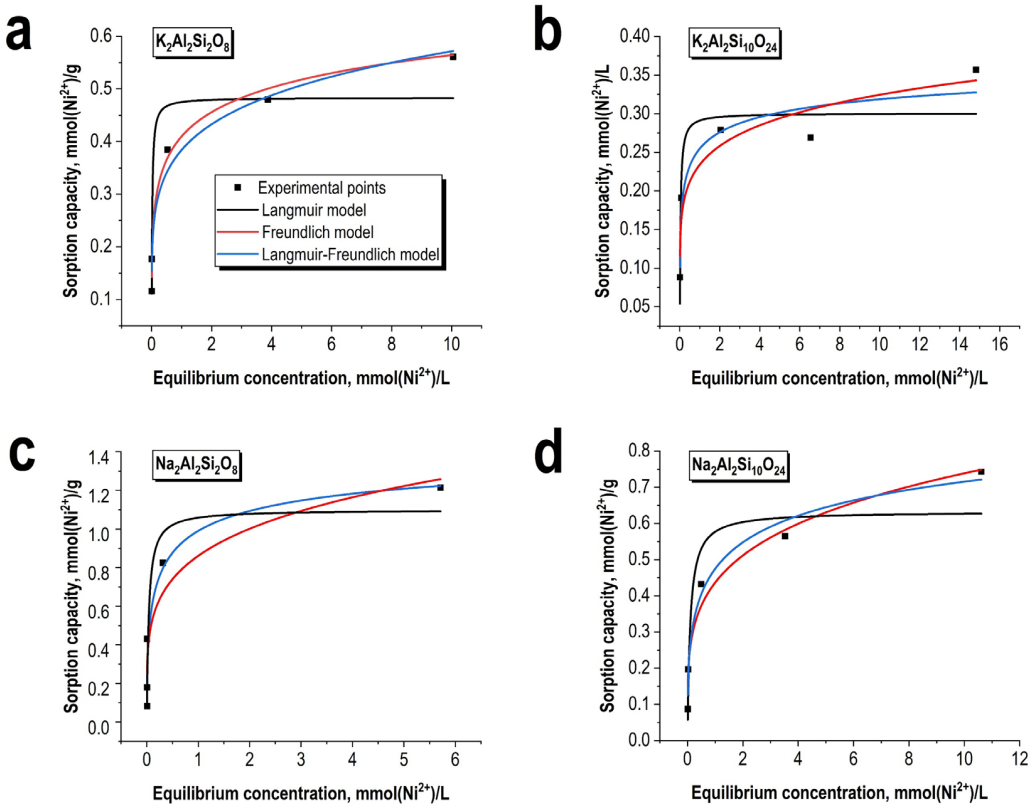

Figure 4. Isotherms of Ni^{2+} sorption on obtained aluminosilicate materials: (**a**) $K_2Al_2Si_2O_8$, (**b**) $K_2Al_2Si_{10}O_{24}$, (**c**) $Na_2Al_2Si_2O_8$, (**d**) $Na_2Al_2Si_{10}O_{24}$.

Table 2. Parameters of isotherm models for Ni^{2+} sorption on obtained aluminosilicate materials.

Isotherm Model	Parameters	$K_2Al_2Si_2O_8$	$K_2Al_2Si_{10}O_{24}$	$Na_2Al_2Si_2O_8$	$Na_2Al_2Si_{10}O_{24}$
Freundlich	n	0.17 ± 0.02	0.14 ± 0.03	0.22 ± 0.06	0.23 ± 0.03
	K_f	0.38 ± 0.02	0.23 ± 0.02	0.86 ± 0.12	0.44 ± 0.03
	R^2	0.98	0.92	0.87	0.97
Langmuir	Q^l_{max}, mmol/g	0.48 ± 0.04	0.30 ± 0.03	1.10 ± 0.19	0.63 ± 0.07
	K_l, L/mmol	58 ± 29	31 ± 20	26 ± 18	10.3 ± 8.5
	R^2	0.91	0.85	0.82	0.89
Langmuir-Freundlich	Q^l_{max}, mmol/g	1.00 ± 0.56	0.44 ± 0.11	1.52 ± 0.90	1.13 ± 0.60
	K_{lf}, L/mmol	0.69 ± 0.72	1.54 ± 1.18	1.89 ± 0.86	0.72 ± 0.76
	m	0.27 ± 0.09	0.34 ± 0.12	0.46 ± 0.33	0.38 ± 0.15
	R^2	0.99	0.99	0.90	0.98

The isotherm shapes correspond to H-type according to Giles classification, characterized by a distinctive vertical initial segment. This indicates uniform occupation of sorption-active sites as the concentration of Ni^{2+} ions increases in solution. Such adsorption isotherm type is characteristic of ion exchange processes and chemisorption [30–32]. The equilibrium adsorption data are more accurately described by the Langmuir-Freundlich

model rather than the Langmuir model (Table 2), confirming the presence of multiple adsorption-active sites and the complex nature of the adsorption mechanism. At high concentrations, the adsorption isotherm exhibited a gradual plateau, indicating a shift in the dominant adsorption process.

The experimental sorption capacity, as well as the maximum theoretical capacity calculated from Langmuir and Langmuir-Freundlich equations, decreases with increasing Si/Al ratio from 1 to 5 (Table 2). This decrease in sorption capacity is inversely proportional to the increase in specific surface area (Table 1) but directly proportional to the content of exchangeable sodium and potassium ions (Table 1). This observation suggests that chemisorption play the most significant role in nickel adsorption, while physical adsorption makes a relatively minor contribution. The capacity of sodium-substituted samples consistently exceeds that of potassium-substituted samples in all cases. Given similar quantitative content of these ions in the obtained sorbents, this difference is attributed to stronger binding of potassium compared to sodium. The $Na_2Al_2Si_2O_8$ sample demonstrates the highest efficiency in terms of sorption capacity.

To determine the rate-limiting step and evaluate diffusion parameters of Ni^{2+} adsorption on the obtained materials, kinetic characteristics were investigated. The general form of experimental adsorption kinetics data along with fitting curves is presented in Figure 5, and the parameters of main kinetic models are summarized in Table 3.

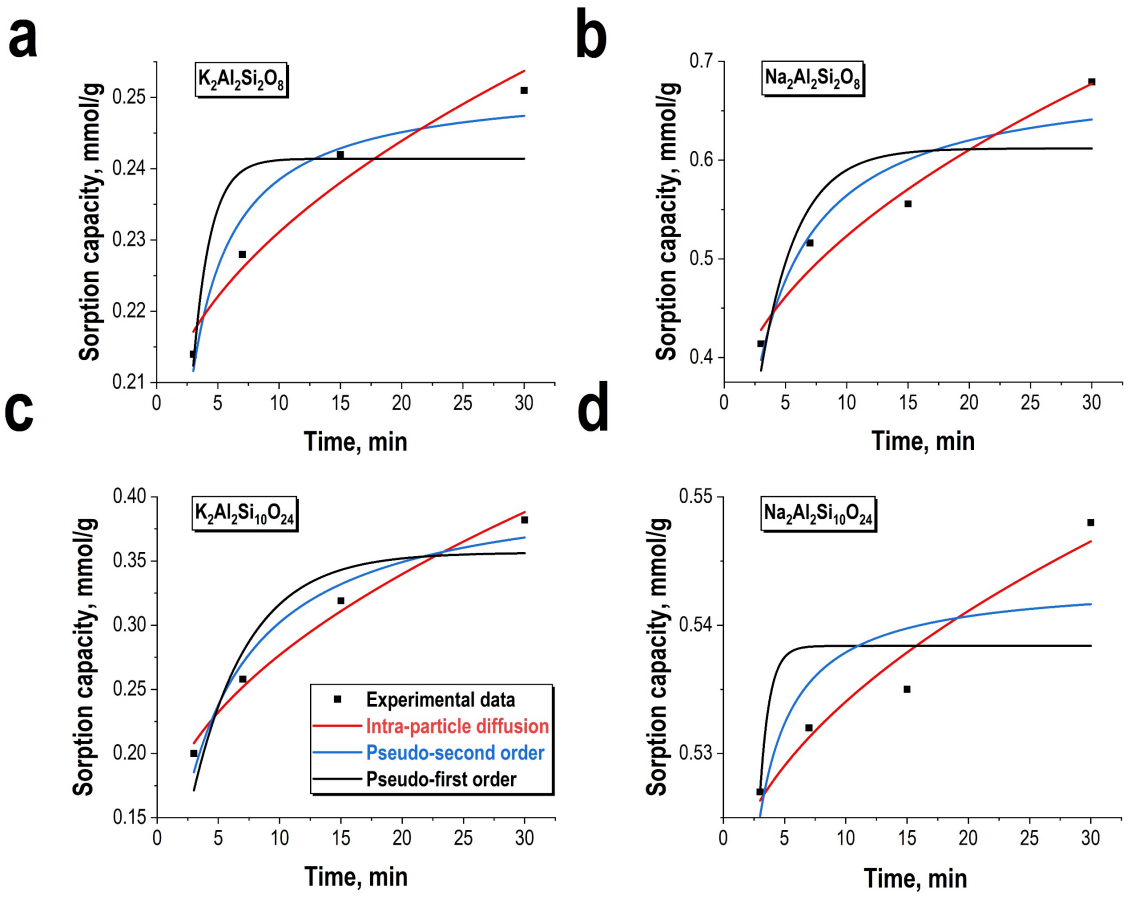

Figure 5. Kinetic curves of Ni^{2+} sorption on obtained aluminosilicate materials: (**a**) $K_2Al_2Si_2O_8$, (**b**) $Na_2Al_2Si_2O_8$, (**c**) $K_2Al_2Si_{10}O_{24}$, (**d**) $Na_2Al_2Si_{10}O_{24}$.

Table 3. Parameters of kinetic models for Ni^{2+} sorption on obtained aluminosilicate materials.

Kinetics Model	Parameters	$K_2Al_2Si_2O_8$	$K_2Al_2Si_{10}O_{24}$	$Na_2Al_2Si_2O_8$	$Na_2Al_2Si_{10}O_{24}$
Lagergren pseudo-first order	Q_{max}, mmol/g	0.241 ± 0.007	0.36 ± 0.03	0.61 ± 0.05	0.54 ± 0.01
	K_1, 1/min	0.71 ± 0.14	0.22 ± 0.06	0.33 ± 0.11	1.29 ± 0.28
	R^2	0.71	0.86	0.74	0.60
Ho pseudo-second order	Q_{max}, mmol/g	0.252 ± 0.004	0.41 ± 0.03	0.68 ± 0.05	0.54 ± 0.01
	K, mmol/g·min	6.9 ± 1.4	0.66 ± 0.19	0.66 ± 0.27	17.48 ± 8.99
	R^2	0.95	0.96	0.90	0.67
Morris-Webber intra-particle diffusion	K, mmol (g·min½)	0.0098 ± 0.0015	0.048 ± 0.004	0.067 ± 0.008	0.0054 ± 0.0008
	C, mmol/g	0.200 ± 0.006	0.120 ± 0.010	0.310 ± 0.030	0.517± 0.003
	R^2	0.95	0.98	0.97	0.95

The obtained coefficients (Table 3) reveal complex kinetic relationships. Notably, there is an increase in sorption capacity, determined by pseudo-first and pseudo-second-order equations, for sodium-substituted samples. With increasing Si/Al ratio, sorption capacity also increased for K-substituted samples while remaining relatively constant for Na-substituted ones. These patterns in sorption capacity changes confirm the conclusions drawn from equilibrium adsorption isotherm analysis.

The Morris-Weber intraparticle diffusion kinetic model best describes the experimental data (R^2 values reach 0.95–0.98—Table 3). However, non-zero values of coefficient C, reflecting boundary layer thickness, are noteworthy. Thus, while intraparticle diffusion processes most significantly influence nickel adsorption rate on aluminosilicates, chemisorption in the boundary layer also affect the final stage [33,34]. The pseudo-second-order model shows the second-highest determination coefficients, indicating the chemical nature of the adsorption process [35].

The rate constant of the pseudo-second-order kinetic equation for $K_2Al_2Si_2O_8$ was ten times higher than for $K_2Al_2Si_{10}O_{24}$, attributed to increased chemical reaction rates in the final adsorption stage. However, the intraparticle diffusion rate of nickel ions in the porous structure of $K_2Al_2Si_{10}O_{24}$ is considerably higher than in $K_2Al_2Si_2O_8$.

Comparison of chemisorption reaction rates between $Na_2Al_2Si_2O_8$ and $Na_2Al_2Si_{10}O_{24}$ is not feasible as the experimental dependencies for $Na_2Al_2Si_{10}O_{24}$ do not fit accurately to the nonlinear pseudo-second-order equations ($R^2 = 0.67$). However, diffusion characteristics of these samples can be compared due to acceptable determination coefficients ($R^2 > 0.95$). $Na_2Al_2Si_2O_8$ shows an order of magnitude higher intraparticle diffusion coefficient K compared to $Na_2Al_2Si_{10}O_{24}$. This can be attributed to lower specific surface area (Table 1) and higher particle size (Figure 2), which reduces the overall diffusion path. Moreover, the coefficient value K = 0.067 mmol/(g·min½) for $Na_2Al_2Si_2O_8$ is the highest among all studied aluminosilicate samples, which, combined with the highest sorption capacity, indicates this sample's optimality.

Overall, the observed dependencies of nickel diffusion rates and chemisorption reactions demonstrate complex behavior: both the type of ion Na^+ (K^+) and Si/Al ratio significantly influence the process, determining porous structure and number of active sorption sites. Therefore, future research should focus on investigating kinetic dependencies across a broader range of Si/Al ratios.

To evaluate the sorption selectivity of the obtained materials for real industrial conditions, sorption-selective characteristics were investigated under conditions of treating model and real solutions with varying content of interfering ions (Table 4). Seawater contains high concentrations of alkali metals, groundwater is characterized by low total salt content, while the model industrial wastewater solution contains, in addition to nickel, ions of other heavy metals (lead, copper, manganese) that are also prone to adsorption on

aluminosilicate surfaces [36,37]. In all cases (Table 4), an increase in sorption characteristics of $Na_2Al_2Si_2O_8$ compared to $K_2Al_2Si_2O_8$ was observed, confirming previously drawn conclusions. Under groundwater treatment conditions, which has low concentrations of interfering ions, high removal efficiencies were observed: 94% and 90% for $Na_2Al_2Si_2O_8$ and $K_2Al_2Si_2O_8$, respectively. Nickel extraction from seawater containing large amounts of interfering alkali metal cations can be performed achieving lower removal efficiencies of 45% and 35% and reduced sorption capacity to 7.0 mg/g and 6.1 mg/g for $Na_2Al_2Si_2O_8$ and $K_2Al_2Si_2O_8$. Model industrial wastewater solutions are treated notably worse, with removal efficiencies of 16% and 8%, respectively, and sorption capacity significantly decreases to 1.6–3.0 mg/g. Overall, the obtained data (Table 4) indicate that $Na_2Al_2Si_2O_8$ material can effectively remove Ni^{2+} from liquid media with low content of interfering cations. Under conditions of treating liquid media with high content of competing alkali metal cations (seawater), $Na_2Al_2Si_2O_8$ retains up to 48% of the original sorption parameters for sorption capacity and removal efficiency. In liquid media containing other heavy metals (Pb, Zn, Cu), the application of $Na_2Al_2Si_2O_8$ sorbent is limited due to competitive adsorption processes of these ions together with Ni^{2+}.

Table 4. Sorption capacity and nickel removal efficiency from model and real solutions using the synthesized aluminosilicate materials.

Solution Type	Solution Origin	Solution Properties	Solution Composition	$Na_2Al_2Si_2O_8$ Sorption Characteristics	$K_2Al_2Si_2O_8$ Sorption Characteristics
Seawater contaminated with Ni^{2+}	Natural Seawater spiked with Ni^{2+}	pH = 7.17	C(Ni) = 17.4 mg/L	Q = 7.9 mg(Ni^{2+})/g R = 45%	Q = 6.1 mg(Ni^{2+})/g R = 35%
Groundwater contaminated with Ni^{2+}	Natural groundwater spiked with Ni^{2+}	pH = 6.88	C(Si) = 4.5 mg/L C(Ca) = 3.4 mg/L C(Na) = 2.1 mg/L C(Mg) = 0.8 mg/L C(K) = 0.3 mg/L C(Ni) = 19.6 mg/L	Q = 18.4 mg(Ni^{2+})/g R = 94%	Q = 17.7 mg(Ni^{2+})/g R = 90%
Industrial wastewater	Model solution	pH = 3.33	C(Cu) ≈ 20 mg/L C(Pb) ≈ 20 mg/L C(Mn) ≈ 20 mg/L C(Ni) = 18.9 mg/L	Q = 3.0 mg(Ni^{2+})/g R = 16%	Q = 1.6 mg(Ni^{2+})/g R = 8%

3.3. Mechanism of Adsorption Interaction Between Ni^{2+} and Aluminosilicate Surface

To elucidate the adsorption mechanism, material surfaces before and after nickel saturation were investigated using XPS. Survey XPS spectra and detailed scans of core electronic levels of main structural elements are presented in Figure 6, while quantitative relationships of electronic states before and after adsorption are shown in Tables 5 and 6, respectively. Ni 2p 3/2 peaks can be reliably deconvoluted into electronic states only in Ni-$Na_2Al_2Si_2O_8$ and Ni-$K_2Al_2Si_2O_8$ samples, while detailed analysis of this spectral region is not feasible for Ni-$Na_2Al_2Si_{10}O_{24}$ and Ni-$K_2Al_2Si_{10}O_{24}$ samples due to low surface nickel concentration. Therefore, for samples with high Si/Al ratio, analysis focused on electronic states of other structural elements involved in nickel ion binding.

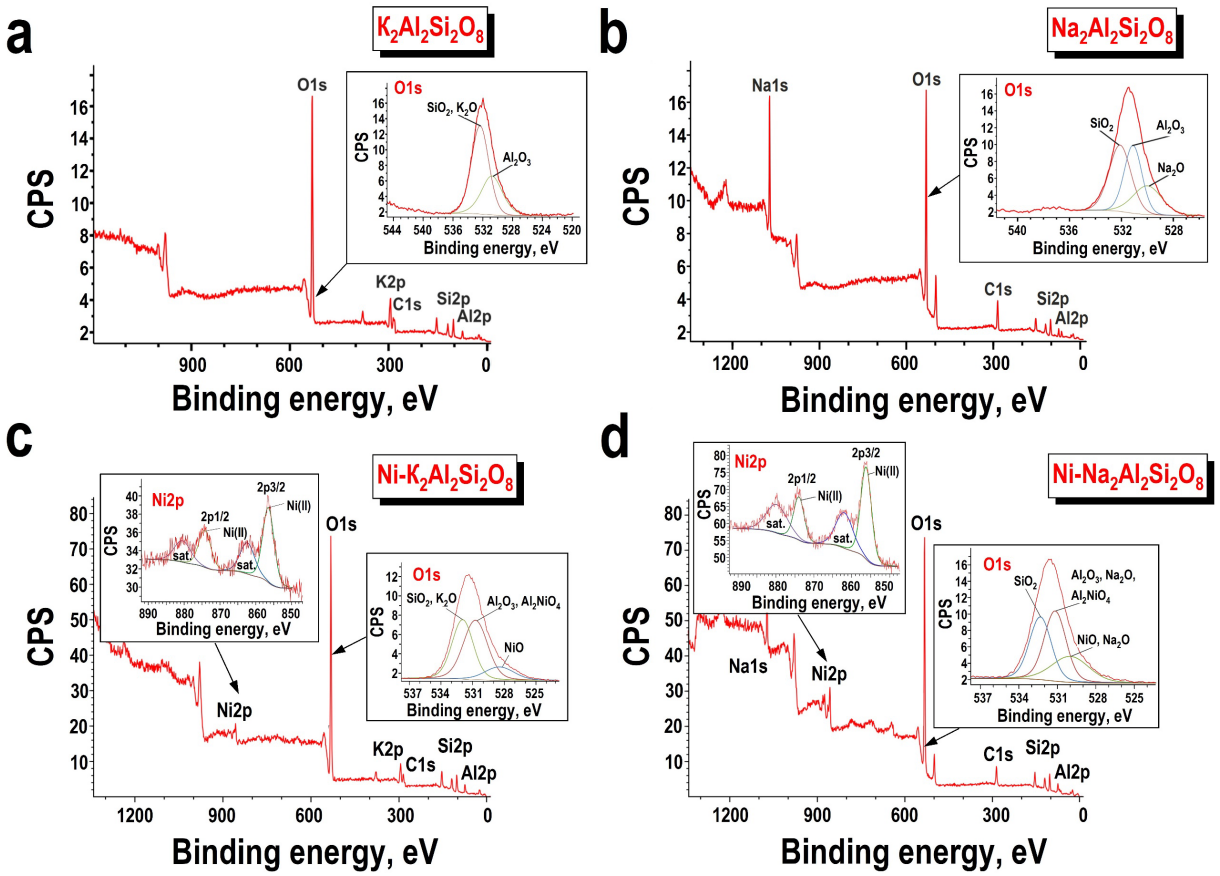

Figure 6. XPS spectra for initial and Ni^{2+}-saturated aluminosilicate materials: (**a**) $K_2Al_2Si_2O_8$, (**b**) $Na_2Al_2Si_2O_8$, (**c**) Ni-$K_2Al_2Si_2O_8$, (**d**) Ni-$Na_2Al_2Si_2O_8$.

Table 5. XPS electronic states of elements in initial K-substituted and Ni-saturated aluminosilicates.

Characteristic Line	Chemical State *	$K_2Al_2Si_2O_8$	Ni-$K_2Al_2Si_2O_8$	$K_2Al_2Si_{10}O_{24}$	Ni-$K_2Al_2Si_{10}O_{24}$
O 1s	SiO_2, KO_2	532.1 eV	532.1 eV (22.44%)	532.4 eV (35.99%)	532.3 eV (38.61%)
	Al_2O_3, Al_2NiO_4	530.7 eV	530.9 eV (25.65%)	530.9 eV (18.97%)	530.7 eV (18.18%)
	NiO	-	528.7 eV (7.2%)	-	-
Si 2p	SiO_2	n/d	102.8 eV (12.09%)	103.3 eV (18.21%)	103.1 eV (20.42%)
	SiC		101.2 eV (6.56%)	101.9 eV (8.11%)	103.6 eV (7.69%)
Al 2p	Al_2NiO_4	n/d	75.2 eV (6.23%)	-	-
	Al_2O_3		74.4 eV (9.31%)	74.7 eV (4.28%)	74.6 eV (3.57%)
K 2p 3/2	K_2O	n/d	293.7 eV (4.06%)	294.0 eV (1.62%)	293.8 eV (1.16%)
C 1s	CnHm, C	n/d	285.0 eV (2.97%)	285.0 eV (7.56%)	285.0 eV (7.55%)
	SiC		282.0 eV (2.33%)	282.0 eV (5.26%)	282.5 eV (2.82%)
Ni 2p 3/2	NiO, Al_2NiO_4	-	856.6 eV (1.16%)	-	n/d

* the elemental composition is given in atomic percentages (at.%).

Table 6. XPS electronic states of elements in initial Na-substituted and Ni-saturated aluminosilicates.

Characteristic Line	Chemical State *	$Na_2Al_2Si_2O_8$	Ni-$Na_2Al_2Si_2O_8$	$Na_2Al_2Si_{10}O_{24}$	Ni-$Na_2Al_2Si_{10}O_{24}$
O 1s	SiO_2	532.1 eV (18.20%)	532.3 eV (18.40%)	532.0 eV (33.17%)	532.0 eV (32.10%)
	Al_2O_3, Al_2NiO_4	531.1 eV (16.75%)	531.2 eV (20.50%)	531.1 eV (3.31%)	531.7 eV (4.38%)
	NiO, Na_2O	530.0 (8.30%)	530.0 eV (12.90%)	530.1 eV (15.36%)	530.1 eV (11.27%)
Si 2p	SiO_2	102.5 eV (11.36%)	102.6 eV (10.41%)	102.8 eV (15.49%)	103.4 eV (12.56%)
	SiC	101.3 eV (5.17%)	101.2 eV (5.04%)	101.4 eV (9.26%)	102.5 eV (9.50%)
Al 2p	Al_2NiO_4	-	74.9 eV (4.09%)	-	-
	Al_2O_3	74.5 eV (7.64%)	74.2 eV (4.67%)	74.4 eV (1.37%)	74.5 eV (2.74%)
	SiO_2 (Al_2O_3)	73.2 eV (3.47%)	-	73.3 eV (1.58%)	-
Na 1s	Na_2O	1072.3 eV (3.83%)	1072.1 eV (2.17%)	1072.3 eV (1.28%)	1072.5 eV (0.97%)
	Na (org.)	1070.7 eV (0.91%)	1070.4 eV (0.52%)	1071.0 eV (0.84%)	1071.1 eV (0.49%)
C 1s	$NaC_2H_3O_2$	288.1 eV (3.42%)	288.9 eV (1.38%)	289.2 eV (0.84%)	287.3 eV (2.73%)
	CnHm, C	285.0 eV (15.44%)	285.0 eV (9.11%)	285.0 eV (7.58%)	285.0 eV (12.52%)
	SiC	283.2 eV (5.51%)	283.3 eV (7.22%)	283.1 eV (8.22%)	282.7 eV (10.65%)
	CO			287.1 eV (1.70%)	
Ni 2p 3/2	NiO, Al_2NiO_4	-	856.2 (3.59%)	-	n/d

* the elemental composition is given in atomic percentages (at.%).

Post-adsorption nickel exhibited a single electronic state at 856.2–856.6 eV (Figure 6, Tables 5 and 6), characteristic of divalent Ni^{2+} ions in octahedral coordination. The decrease in Na^+ and K^+ ion concentrations indicates ion exchange with Ni^{2+} as possible adsorption mechanism. After sorption saturation, the deconvolution of O 1s electronic states changes: (i) in Ni-$K_2Al_2Si_2O_8$ sample, a new component appears at 528.7 eV, attributed to direct oxygen-nickel bonding (NiO), while the hydroxyl group component at 532.1 eV decreases; (ii) in Ni-$Na_2Si_2O_8$ sample, the intensity of the 528.7 eV component also increases; (iii) in Ni-$Na_2Al_2Si_{10}O_{24}$ and Ni-$K_2Al_2Si_{10}O_{24}$ samples, conversely, the intensity of hydroxyl group component at 532.0–532.4 eV increases.

These differences may be attributed to the dominance of chemisorption processes and formation of new compounds in samples with low Si/Al ratio (1), while samples with high Si/Al ratio (5) show formation of surface-coordinated inner-sphere and outer-sphere complexes with hydroxyl groups [38]. For Al 2p in Ni-$K_2Al_2Si_2O_8$ and Ni-$Na_2Al_2Si_2O_8$ samples, a new component appears at 74.9–75.2 eV, indicating chemisorption processes with new phase formation. This assumption is further supported by surface morphology and XRD/FTIR after sorption (Figure 7). The distribution of electronic states for other elements' peaks (Si 2p, K 2p 3/2, and Na 1s) shows no significant changes after adsorption.

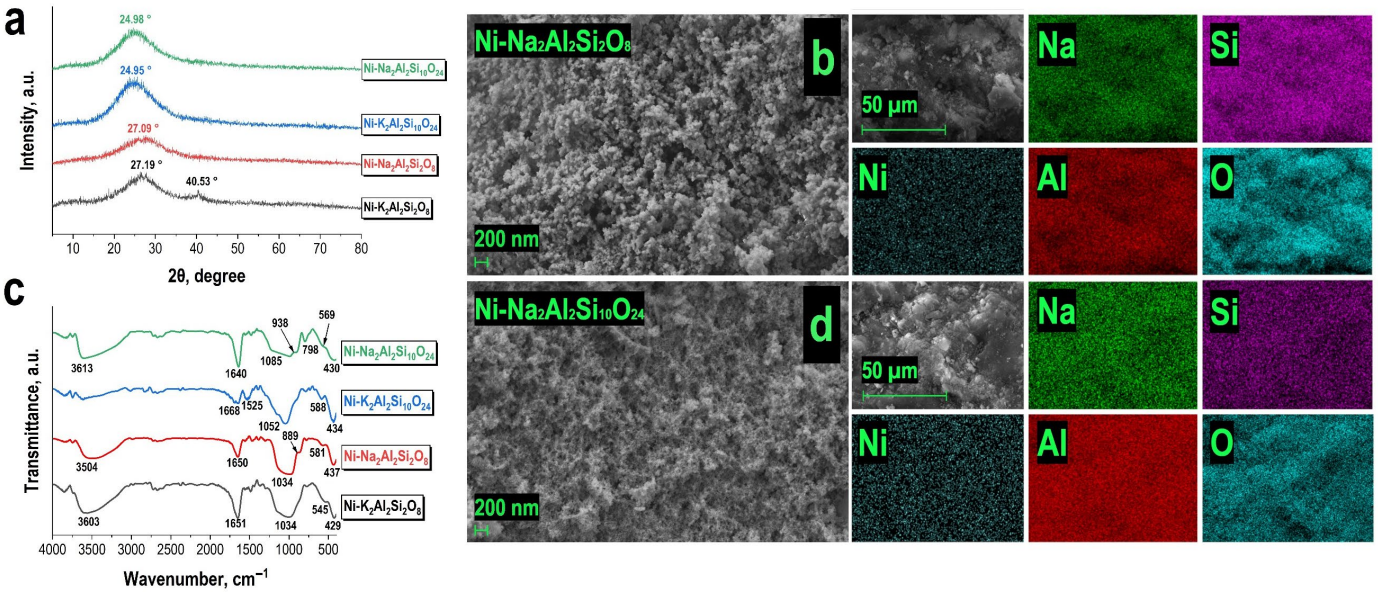

Figure 7. Physicochemical characterization of Ni-saturated aluminosilicate materials: (**a**) XRD patterns, (**b**) FTIR spectra, (**c**,**d**) SEM images and EDS elemental distribution maps.

For identifying the dominant adsorption mechanisms, a comprehensive approach using multiple complementary analytical methods is important [39,40]. In this regard, within the framework of this study, in addition to XPS, XRD, FTIR, and SEM-EDS microscopy were used to investigate the nickel-saturated samples (Figure 7).

The diffractograms of nickel-saturated $K_2Al_2Si_2O_8$, $K_2Al_2Si_{10}O_{24}$, and $Na_2Al_2Si_{10}O_{24}$ (Figure 7a) are practically indistinguishable from the diffractograms of the initial materials. For the $K_2Al_2Si_2O_8$ sample, the appearance of new maxima in the $2\theta = 40.53°$ region is noticeable, indicating the formation of new nanocrystalline phases on the material surface. However, due to the small coherent scattering domain size for the newly formed phases, significant broadening of the diffraction maxima is also observed, which prevents their precise identification by XRD data. According to available literature data, silicate materials can sorb Ni^{2+} with the formation of two types of compounds: (1) nickel hydroxides in α- and β-forms, and (2) layered double hydroxides (LDH) of nickel-aluminum [38]. Characteristic maxima of LDH and α-$Ni(OH)_2$ in the low-angle diffraction region are absent, which may indicate the formation of the β-form of nickel hydroxide or a mixed compound (the most intense X-ray maxima for hexagonal β-$Ni(OH)_2$ ICDD PDF 00-014-0117 lie in the 38° and 19° regions). However, for precise confirmation of this assumption, it is necessary to apply advanced methods for analyzing the local environment of nickel, particularly X-ray absorption spectroscopy in accordance with the recommendations [38].

FTIR spectra after sorption saturation of nanostructured aluminosilicates with Ni^{2+} ions (Figure 7d) demonstrate changes confirming the proposed adsorption mechanisms. First, a shift toward higher frequencies of the absorption band for asymmetric stretching vibrations of Si-O-Al bonds (up to 1034–1085 cm^{-1}) is noticeable. This frequency shift occurs due to the change in the local electronic environment around the Si-O-Al framework when nickel ions replace the original exchangeable cations. The substitution of smaller, more highly charged Ni^{2+} ions for larger monovalent cations (Na^+ or K^+) at exchange sites results in stronger electrostatic interactions with the aluminosilicate framework, thereby increasing the bond strength and vibrational frequency of the Si-O-Al bonds. This spectroscopic evidence clearly indicates the occurrence of ion exchange with nickel substitution at sodium or potassium exchange sites [41–43]. For the nickel-saturated Ni-$K_2Al_2Si_2O_8$ sample, a relative decrease in transmittance (%) in the low-frequency region of 429–545 cm^{-1}

is observed, which is probably caused by the overlap of Ni-O bond absorption bands and absorption bands of bridging Si-O-Si bonds [44]. Characteristic absorption bands of β-$Ni(OH)_2$, particularly the narrow band at 3650 cm^{-1}, are nevertheless absent in the FTIR spectra of this sample, indicating a mixed disordered nature of the nickel hydroxide, poorly developed crystalline structure, and the presence of water and other adsorbed molecules in its interlayer space. For practically all samples after nickel saturation, the intensity of the band at 1640–1651 cm^{-1} significantly increases, indicating the presence of bound water. Such changes may be caused by surface complexation or the formation of hydrated precipitates on the material surface. The increase in intensity of the absorption band at 3500–3613 cm^{-1} also indicates an increase in bound water and/or hydroxyl group content.

SEM images of nickel-saturated aluminosilicates (Figure 7c,d) demonstrate morphological changes toward more finely dispersed particles. These changes can be attributed to nickel hydroxide precipitation on the aluminosilicate surface. EDS elemental distribution maps (Figure 7c,d) indicate the preservation of homogeneous composition regarding main structural elements and confirm uniform distribution of adsorbed nickel. Therefore, the adsorption of nickel ions from liquid media results in the formation of a nanostructured composite consisting of novel nickel-containing phases and the original aluminosilicate structure.

The combination of XRD, SEM-EDS, and FTIR data (Figure 7) indicates a complex nature of the nickel adsorption mechanism involving a combination of ion exchange, formation of new phases (presumably nickel hydroxide $Ni(OH)_2$), and surface complexation. For $K_2Al_2Si_2O_8$, clear evidence of surface precipitation of nickel compounds was found. XPS data complementarily confirm these assumptions and indicate that for samples with low Si/Al = 1 ratio, chemisorption with formation of new surface-precipitated phases plays a significant role, while for samples with high Si/Al ratio, surface complexation predominates.

Figure 8 presents the potential mechanisms for nickel ion (Ni^{2+}) adsorption on the surface of nanostructured aluminosilicates. Based on the results of this work, as well as data from previously conducted studies [20], the functional groups on the aluminosilicate surface are represented by hydroxyl (-OH) groups, deprotonated hydroxyl centers ($-O^-$), and alkali metal-substituted groups (-ONa, -OK). Ni^{2+} ions in aqueous medium acquire a hydration shell and exist in the form of octahedrally coordinated complex ion $Ni(H_2O)_6^{2+}$ [45]. Ion exchange (Figure 8(1)) can proceed through alkali metal-substituted hydroxyl groups (-ONa, -OK), whereby newly formed sites of localized excess negative charge ($-O^-$) electrostatically bind with hydrated nickel ions, leading to the formation of outer-sphere surface complexes (Figure 8(2)). XPS elemental analysis data (Table 5) unambiguously confirm alkali metal substitution during nickel adsorption on aluminosilicate samples. An alternative form of ion exchange may involve the loss of the hydration shell by $Ni(H_2O)_6^{2+}$ ions and incorporation of Ni^{2+} ions into the aluminosilicate crystal structure [46]. Outer-sphere complexes can be monodentate (Figure 8(3a)) and bidentate (Figure 8(3b)). [47]. The main difference from outer-sphere complexes lies in the shorter distance from the Ni center to the aluminosilicate surface. In inner-sphere complexes, one or two oxygen atoms in the nickel coordination sphere are directly bonded to the aluminosilicate surface. XPS results (Table 5) and FTIR spectroscopy data (Figure 7) confirm the involvement of surface complexes in the nickel adsorption mechanism on nanostructured aluminosilicates. Finally, surface precipitation in the form of $Ni(OH)_2$ (Figure 8(4)) has been reported by several authors [38] as the final stage of inner-sphere complexation with the formation of a new crystalline structure on the material surface. This assumption is also supported by ab initio molecular modeling results presented in the study [48]. Within the current study, XRD analysis of $K_2Al_2Si_2O_8$ confirmed the formation of new phases (Figure 7a), while most investigated samples demonstrate surface morphology changes that may be attributed

to surface precipitation (Figure 7b,d). Thus, according to data from multiple laboratory methods employed in this work, nickel adsorption on aluminosilicate surfaces is a complex process governed by the contribution of each of the mechanisms described.

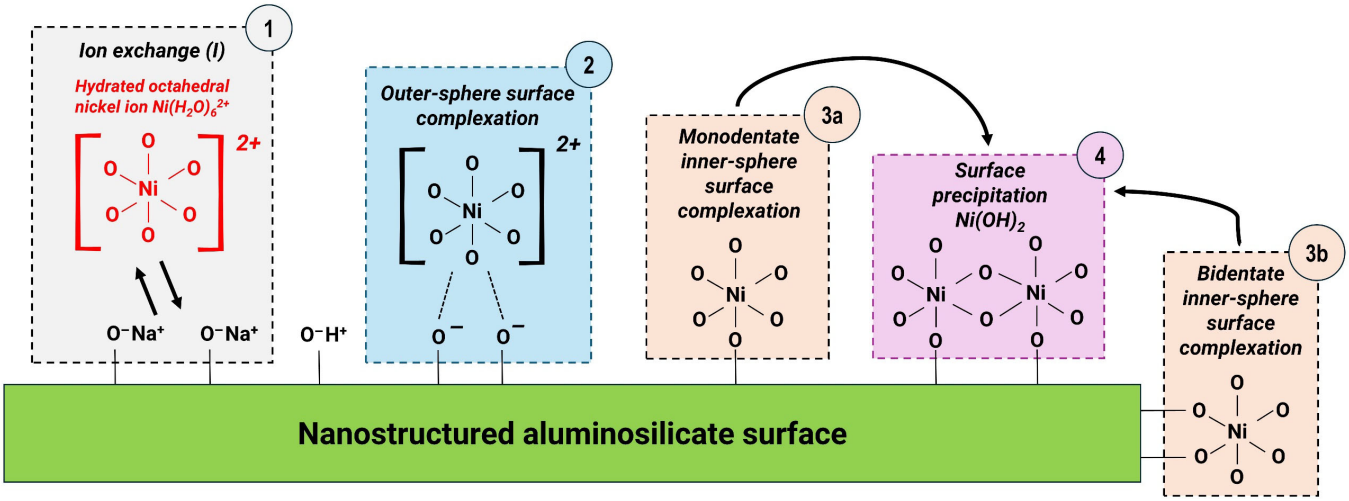

Figure 8. Potential mechanisms for nickel (Ni^{2+}) adsorption on the synthesized aluminosilicates.

3.4. Comparative Sorption Capacity Evaluation

To evaluate the potential of the obtained material as a sorbent for Ni^{2+} removal, the batch sorption capacity was compared with other silicate materials proposed by the global scientific community as sorbents (Table 7). Among the compared samples, the highest nickel sorption capacities were demonstrated by silicate materials based on paper waste (266.5 mg/g) [49], bentonite-based geopolymer (1227.2 mg/g) [15] and clinoptilolite-chitosan composite (247.1 mg/g) [50]. Most proposed materials exhibited sorption capacities in the range of 20–80 mg/g. The nanostructured aluminosilicates obtained in this study demonstrate a sorption capacity of 64.6 mg/g, which is comparable to the average level of this parameter. The simplicity and cost-effectiveness of synthesis, potential for industrial waste utilization in material production [51], and favorable adsorption kinetic characteristics make these materials particularly promising for practical applications.

Table 7. Sorption Capacity of Silicate-Based Materials for Ni^{2+} Removal.

Sorption Material	Characterization of the Material	Sorption Capacity	Ref.
Zeo/PVA/SA NC	Nanocomposite based on polyvinyl alcohol, sodium alginate and natural zeolite (RaaTec-Zeolite supplements Company, Helsingborg, Sweden)	47.619 mg/g	[52]
Clinoptilolite (Sokyrnytsa, Sokyrnyansky deposit, Ukraine)	Clinoptilolite rock (~75% clinoptilolite). Associated minerals: quartz, calcite, biotite, muscovite, chlorite, montmorillonite	15.55 mg/g	[53]
Rectorite (Zhongxiang, Hubei Province, China)	Na-rectorite sample $Na{\cdot}Al_4[Si,Al]_8O_{20}[OH]_4{\cdot}xH_2O$ (S_{BET} = 11.9 m^2/g)	6.3–10.2 mg/g (1.08–1.74·10^{-4} mol/g)	[54]
Calcined paper sludge	Dry-milled and calcined (500–900 °C) paper sludge containing compounds in $CaO(MgO)$-Al_2O_3-SiO_2 system	85.1–266.5 mg/g (1.45–4.54 mmol/g)	[49]
Palygorskite-based composite membranes	Bicomponent membranes based on polyvinylidene fluoride (PVDF) and hyperbranched polyamidoamine-palygorskite	124.28 mg/g	[55]
Montmorillonite (Ugwuoba, Nigeria)	Acid-treated montmorillonite (0.5–2.5 M H_2SO_4)	4.0 mg/g	[56]
Silica clay, Mojallali Co., (Isfahan, Iran), modified with biopolymers	Alginate-encapsulated silica clay (S_{BET} = 497 m^2/g)	21.1 mg/g	[57]
Bentonite nanoclay-based geopolymer	Bentonite clay-based geopolymer modified with Fe_3O_4 nanoparticles (geopolymer/Fe_3O_4 ratio = 13)	1227.2 mg/g	[15]

Table 7. *Cont.*

Sorption Material	Characterization of the Material	Sorption Capacity	Ref.
Polymer-modified natural aluminosilicates (Eastern Transbaikalia, Irkutsk, Russia)	Aluminosilicates modified with poly-1-vinylimidazole (PVIM) and poly-4-vinylpyridine (PVP)	16.96 mg/g (0.289 mmol/g) 14.73 mg/g (0.251 mmol/g)	[58]
Modified natural aluminosilicates (Eastern Transbaikalia Irkutsk, Russia)	Aluminosilicate (75% calcium heulandite $Ca[Al_2Si_7O_{18}]\cdot 6H_2O$ and 25% K-feldspar $KAlSi_3O_8$) modified with N,N′-bis(3-triethoxysilylpropyl)thiocarbamide	79.6 mg/g (1.36 mmol/g)	[59]
Clinoptilolite-based composite (Cluj County, Romania)	Clinoptilolite-chitosan composite from volcanic tuffs	247.1 mg/g 4.209 mmol/g	[50]
Synthetic zeolite X from coal ash	Zeolite X (S_{BET} = 242.04 m^2/g) synthesized by alkaline fusion with NaOH at 600 °C (90 min) followed by hydrothermal treatment at 100 °C (24 h)	79.2 mg/g (1.35 mmol/g)	[60]
Zeolite (Yagodninsky deposit, Nachiki, Kamchatka, Russia)	Zeolitic tuffs containing clinoptilolite (70%), mordenite (10%), and cristobalite, quartz, mica, clay minerals (20%)	2.34 mg/g	[61]
Nanostructured K and Na aluminosilicates	Nanostructured potassium and sodium aluminosilicates with varying Si/Al ratios: $M_2Al_2Si_xO_{2(x+4)}\cdot nH_2O$ (M = K^+, Na^+; x = 2, 10) and $Na_2Al_2Si_{2k}O_{2(2k+2)}\cdot nH_2O$ (k = 1–5)	64.6 mg/g (1.1 mmol/g)	this study

4. Conclusions

To address nickel removal from heavy industry wastewater, new sorption materials based on potassium- and sodium-substituted nanostructured aluminosilicates were developed. A comparative evaluation of sorption capacity, kinetic characteristics, and sorption mechanisms was conducted.

All synthesized materials exhibited an X-ray amorphous structure due to extremely small crystallite size. While K-substituted aluminosilicates possessed larger specific surface areas, sorption capacity demonstrated an inverse relationship with specific surface area and a direct relationship with alkali metal and Al^{3+} content. According to the proposed complex adsorption mechanism, higher sodium or potassium content correlates with greater ion exchange capacity, while increased aluminum content provides more negatively charged centers for surface complexation and precipitation. The $Na_2Al_2Si_2O_8$ sample showed the highest sorption capacity for Ni(II) at 64.6 mg/g (1.1 mmol/g) and optimal kinetic characteristics.

Investigation of sorption mechanisms revealed the dominant role of chemisorption processes. XPS, XRD, SEM-EDS, and FTIR analyses confirmed that nickel adsorption occurs through ion exchange, surface complexation, and chemisorption with formation of new nickel-containing compounds, resulting in a nanostructured composite interface.

Adsorption selectivity studies revealed that $Na_2Al_2Si_2O_8$ effectively removes Ni^{2+} from groundwater (94% removal efficiency) but shows reduced performance in seawater (45% removal efficiency) and industrial wastewater containing competing heavy metals (16% removal efficiency. The optimal nanostructured material $Na_2Al_2Si_2O_8$ demonstrates promising potential for practical application in nickel removal from wastewater, particularly for solutions with low competing ion content.

Author Contributions: Conceptualization, S.Y. and O.S.; methodology, E.N. and N.I. (Nikita Ivanov); software, E.N. and V.M.; validation, O.S., P.G. and E.P.; formal analysis, E.N., A.K., V.M. and V.I.N.; investigation, E.N., K.B., V.P., V.R., V.A., S.S., N.I. (Natalya Ivanenko) and Y.P.; resources, A.S. and E.P.; data curation, E.N., N.I. (Nikita Ivanov), A.K., V.M. and V.I.N.; writing—original draft preparation, N.I. (Nikita Ivanov); writing—review and editing, O.S., P.G., E.P. and S.Y.; visualization, E.N., N.I. (Nikita Ivanov) and V.M.; supervision, S.Y., O.S., P.G. and E.P.; project administration, E.P. and S.Y.; funding acquisition, A.S. and E.P. All authors have read and agreed to the published version of the manuscript.

Funding: The study of structural properties of materials was carried out within the framework of State Assignment No. FZNS-2024-0013, topic: "X-ray absorption spectroscopy on synchrotron radiation sources for the directed chemical synthesis of functional materials in demand in the nuclear industry". The experimental work on synthesis and atomic absorption determination of nickel in solutions was performed under the state assignment of the Institute of Chemistry, Far Eastern Branch of the Russian Academy of Sciences (FWFN(0205)-2022-0002, theme 2, Section 3).

Data Availability Statement: The experimental data that support the findings of this study are available from the corresponding author upon reasonable request.

Conflicts of Interest: The authors declare no conflicts of interest.

References

1. Qu, J.; Liu, J.; Al-Dhabi, N.A.; Leng, Y.; Yi, J.; Jiang, K.; Xing, W.; Yin, D.; Tang, W. Ni-EDTA Decomplexation and Ni Removal from Wastewater by Electrooxidation Coupled with Electrocoagulation: Optimization, Mechanism and Biotoxicity Assessment. *Sep. Purif. Technol.* **2025**, *376*, 133980. [CrossRef]
2. Lee, M.G.; Kam, S.K.; Lee, C.H. Kinetic and Isothermal Adsorption Properties of Strontium and Cesium Ions by Zeolitic Materials Synthesized from Jeju Volcanic Rocks. *Environ. Eng. Res.* **2021**, *26*, 200127. [CrossRef]
3. Singh, G.; Sharma, S. Heavy Metal Contamination in Fish: Sources, Mechanisms and Consequences. *Aquat. Sci.* **2024**, *86*, 107. [CrossRef]
4. Iqbal Khan, Z.; Ghulam Muhammad, F.; Ahmad, K.; Alwahibi, M.S.; Yang, H.-H.; Ishfaq, M.; Anjum, S.; Ali, K.; Iqbal, K.; Radicetti, E.; et al. Nickel Toxicology Testing in Alternative Specimen from Farm Ruminants in a Urban Polluted Environment. *J. King Saud. Univ.-Sci.* **2024**, *36*, 103520. [CrossRef]
5. Rizwan, M.; Usman, K.; Alsafran, M. Ecological Impacts and Potential Hazards of Nickel on Soil Microbes, Plants, and Human Health. *Chemosphere* **2024**, *357*, 142028. [CrossRef] [PubMed]
6. Erulaş, F.A. Sensitive Determination of Nickel at Trace Levels in Surface Water Samples by Slotted Quartz Tube Flame Atomic Absorption Spectrometry after Switchable Solvent Liquid-Phase Microextraction. *Environ. Monit. Assess.* **2020**, *192*, 272. [CrossRef] [PubMed]
7. Koshy, N.; Singh, D.N. Fly Ash Zeolites for Water Treatment Applications. *J. Environ. Chem. Eng.* **2016**, *4*, 1460–1472. [CrossRef]
8. Bayuo, J.; Rwiza, M.J.; Choi, J.W.; Mtei, K.M.; Hosseini-Bandegharaei, A.; Sillanpää, M. Adsorption and Desorption Processes of Toxic Heavy Metals, Regeneration and Reusability of Spent Adsorbents: Economic and Environmental Sustainability Approach. *Adv. Colloid Interface Sci.* **2024**, *329*, 103196. [CrossRef]
9. Kainth, S.; Sharma, P.; Pandey, O.P. Green Sorbents from Agricultural Wastes: A Review of Sustainable Adsorption Materials. *Appl. Surf. Sci. Adv.* **2024**, *19*, 100562. [CrossRef]
10. Hassan, M.; Naidu, R.; Du, J.; Liu, Y.; Qi, F. Critical Review of Magnetic Biosorbents: Their Preparation, Application, and Regeneration for Wastewater Treatment. *Sci. Total Environ.* **2020**, *702*, 134893. [CrossRef]
11. Godage, N.H.; Gionfriddo, E. Use of Natural Sorbents as Alternative and Green Extractive Materials: A Critical Review. *Anal. Chim. Acta* **2020**, *1125*, 187–200. [CrossRef]
12. Bayuo, J.; Rwiza, M.; Mtei, K. Response Surface Optimization and Modeling in Heavy Metal Removal from Wastewater—A Critical Review. *Environ. Monit. Assess.* **2022**, *194*, 351. [CrossRef]
13. Rostami, M.S.; Khodaei, M.M. Recent Advances in Chitosan-Based Nanocomposites for Adsorption and Removal of Heavy Metal Ions. *Int. J. Biol. Macromol.* **2024**, *270*, 132386. [CrossRef] [PubMed]
14. Villafranca, J.C.; Berton, P.; Ferguson, M.; Clausen, R.; Arancibia-Miranda, N.; Martinis, E.M. Aluminosilicates-Based Nanosorbents for Heavy Metal Removal—A Review. *J. Hazard. Mater.* **2024**, *474*, 134552. [CrossRef] [PubMed]
15. Maleki, A.; Hajizadeh, Z.; Sharifi, V.; Emdadi, Z. A Green, Porous and Eco-Friendly Magnetic Geopolymer Adsorbent for Heavy Metals Removal from Aqueous Solutions. *J. Clean. Prod.* **2019**, *215*, 1233–1245. [CrossRef]
16. Abdel Moamen, O.A.; Murad, G.A.; Hassan, H.S. Experimental and Theoretical Study for the Sorption of Ni^{2+} and Cd^{2+} onto Phosphoryl Functionalized Aluminum Silicate Composite. *Sep. Purif. Technol.* **2024**, *344*, 127186. [CrossRef]
17. Tsai, C.-K.; Doong, R.; Hung, H.-Y. Sustainable Valorization of Mesoporous Aluminosilicate Composite from Display Panel Glasses Waste for Adsorption of Heavy Metal Ions. *Sci. Total Environ.* **2019**, *673*, 337–346. [CrossRef]
18. Yarusova, S.B.B.; Shichalin, O.O.O.; Belov, A.A.A.; Azon, S.A.A.; Buravlev, I.Y.; Golub, A.V.V.; Mayorov, V.Y.; Gerasimenko, A.V.V.; Papynov, E.K.K.; Ivanets, A.I.I.; et al. Synthesis of Amorphous $KAlSi_3O_8$ for Cesium Radionuclide Immobilization into Solid Matrices Using Spark Plasma Sintering Technique. *Ceram. Int.* **2022**, *48*, 3808–3817. [CrossRef]

19. Gordienko, P.S.; Yarusova, S.B.; Shabalin, I.A.; Slobodyuk, A.B.; Nekhlyudova, E.A.; Shichalin, O.O.; Papynov, E.K.; Kuryavyi, V.G.; Polyakova, N.V.; Parot'kina, Y.A. Synthesis of Calcium Aluminosilicates from Nanostructured Synthetic Na Zeolites and Study of Their Sorption Properties. *Russ. J. Inorg. Chem.* **2022**, *67*, 1393–1399. [CrossRef]
20. Nekhliudova, E.A.; Ivanov, N.P.; Yarusova, S.B.; Papynov, E.K.; Shichalin, O.O.; Mayorov, V.Y.; Fedorets, A.N.; Shkuratov, A.L.; Shlyk, D.K.; Gordienko, P.S. Synthesis and Sorption Properties of Nanostructured Sodium Aluminosilicates Differing in Si/Al Ratio. *Inorg. Mater.* **2023**, *59*, 1303–1312. [CrossRef]
21. Al-Ghouti, M.A.; Da'ana, D.A. Guidelines for the Use and Interpretation of Adsorption Isotherm Models: A Review. *J. Hazard. Mater.* **2020**, *393*, 122383. [CrossRef] [PubMed]
22. Wang, J.; Guo, X. Adsorption Kinetic Models: Physical Meanings, Applications, and Solving Methods. *J. Hazard. Mater.* **2020**, *390*, 122156. [CrossRef] [PubMed]
23. Carrio, J.A.G.; Donato, R.K.; Carvalho, A.; Koon, G.K.W.; Donato, K.Z.; Yau, X.H.; Kosiachevskyi, D.; Lim, K.; Ravi, V.; Joy, J.; et al. From 2D Kaolinite to 3D Amorphous Cement. *Sci. Rep.* **2025**, *15*, 1669. [CrossRef] [PubMed]
24. Emminger, Y.H.; Ladner, L.; Ruiz-Agudo, C. Comparative Study of the Early Stages of Crystallization of Calcium Silicate Hydrate (C-S-H) and Calcium Aluminate Silicate Hydrate (C-A-S-H). *Cem. Concr. Res.* **2025**, *193*, 107873. [CrossRef]
25. Yiu, Y.M. Techniques for Structural Investigations (Theory and Experimental). In *Applications of Chalcogenides: S, Se, and Te*; Springer International Publishing: Cham, Switzerland, 2017; pp. 61–104.
26. Bates, S.; Zografi, G.; Engers, D.; Morris, K.; Crowley, K.; Newman, A. Analysis of Amorphous and Nanocrystalline Solids from Their X-Ray Diffraction Patterns. *Pharm. Res.* **2006**, *23*, 2333–2349. [CrossRef]
27. Mozgawa, W.; Król, M.; Barczyk, K. FT-IR Studies of Zeolites from Different Structural Groups. *Chemik* **2011**, *65*, 671–674.
28. Ma, Y.K.; Rigolet, S.; Michelin, L.; Paillaud, J.L.; Mintova, S.; Khoerunnisa, F.; Daou, T.J.; Ng, E.P. Facile and Fast Determination of Si/Al Ratio of Zeolites Using FTIR Spectroscopy Technique. *Microporous Mesoporous Mater.* **2021**, *311*, 110683. [CrossRef]
29. Thommes, M.; Kaneko, K.; Neimark, A.V.; Olivier, J.P.; Rodriguez-Reinoso, F.; Rouquerol, J.; Sing, K.S.W. Physisorption of Gases, with Special Reference to the Evaluation of Surface Area and Pore Size Distribution (IUPAC Technical Report). *Pure Appl. Chem.* **2015**, *87*, 1051–1069. [CrossRef]
30. Kumar, D.; Pandey, L.K.; Gaur, J.P. Metal Sorption by Algal Biomass: From Batch to Continuous System. *Algal Res.* **2016**, *18*, 95–109. [CrossRef]
31. Dragan, E.S.; Apopei Loghin, D.F. Enhanced Sorption of Methylene Blue from Aqueous Solutions by Semi-IPN Composite Cryogels with Anionically Modified Potato Starch Entrapped in PAAm Matrix. *Chem. Eng. J.* **2013**, *234*, 211–222. [CrossRef]
32. Urdiales, C.; Gacitua, M.; Villacura, L.; Pizarro, C.; Escudey, M.; Canales, C.; Antilén, M. Variable Surface Charge of Humic Acid-Ferrihydrite Composite: Influence of Electrolytes on Ciprofloxacin Adsorption. *J. Hazard. Mater.* **2020**, *385*, 121520. [CrossRef] [PubMed]
33. Boughriet, A.; Doyemet, G.; Poumaye, N.; Allahdin, O.; Wartel, M. Insight into Adsorption Kinetics of Cs^{+}, Rb^{+}, Co^{2+}, and Sr^{2+} on a Zeolites-Based Composite: Comprehensive Diffusional Explanation and Modelling. *Appl. Sci.* **2024**, *14*, 3511. [CrossRef]
34. Yang, Y.; Liu, D.; Chen, Y.; He, J.; Li, Q. Mechanistic Study of Highly Effective Phosphate Removal from Aqueous Solutions over a New Lanthanum Carbonate Fabricated Carbon Nanotube Film. *J. Environ. Manag.* **2024**, *359*, 120938. [CrossRef] [PubMed]
35. Rajendran, S.; Priya, A.K.; Senthil Kumar, P.; Hoang, T.K.A.; Sekar, K.; Chong, K.Y.; Khoo, K.S.; Ng, H.S.; Show, P.L. A Critical and Recent Developments on Adsorption Technique for Removal of Heavy Metals from Wastewater-A Review. *Chemosphere* **2022**, *303*, 135146. [CrossRef] [PubMed]
36. Velarde, L.; Nabavi, M.S.; Escalera, E.; Antti, M.-L.; Akhtar, F. Adsorption of Heavy Metals on Natural Zeolites: A Review. *Chemosphere* **2023**, *328*, 138508. [CrossRef]
37. Finish, N.; Ramos, P.; Borojovich, E.J.C.; Zeiri, O.; Amar, Y.; Gottlieb, M. Zeolite Performance in Removal of Multicomponent Heavy Metal Contamination from Wastewater. *J. Hazard. Mater.* **2023**, *457*, 131784. [CrossRef]
38. Mo, X.; Siebecker, M.G.; Gou, W.; Li, W. EXAFS Investigation of Ni(II) Sorption at the Palygorskite-Solution Interface: New Insights into Surface-Induced Precipitation Phenomena. *Geochim. Cosmochim. Acta* **2021**, *314*, 85–107. [CrossRef]
39. Ivanov, N.P.; Shichalin, O.O.; Trigub, A.L.; Rastorguev, V.L.; Nekrasova, N.A.; Provatorova, V.V.; Gnilyak, E.A.; Zaikova, A.R.; Rinchinova, V.B.; Lembikov, A.O.; et al. Optimization of Zn/Al Cationic Ratio in Zn-Al-LDH for Efficient U(VI) Adsorption. *J. Water Process Eng.* **2025**, *69*, 106735. [CrossRef]
40. Akram, M.; Bano, Z.; Bhutto, S.U.A.; Majeed, M.K.; Pan, J.; Li, L.; Xia, M.; Wang, F. Enhanced Nickel (II) Removal from Aqueous Media Using Magnesium-*Punica granatum* Linn Based Adsorbent: Mechanism and Performance. *J. Mol. Liq.* **2025**, *431*, 127808. [CrossRef]
41. Mozgawa, W.; Fojud, Z.; Handke, M.; Jurga, S. MAS NMR and FTIR Spectra of Framework Aluminosilicates. *J. Mol. Struct.* **2002**, *614*, 281–287. [CrossRef]
42. O'Connor, S.J.; MacKenzie, K.J.D.; Smith, M.E.; Hanna, J.V. Ion Exchange in the Charge-Balancing Sites of Aluminosilicate Inorganic Polymers. *J. Mater. Chem.* **2010**, *20*, 10234. [CrossRef]

43. Wang, Y.; Han, F.; Mu, J. Solidification/Stabilization Mechanism of Pb(II), Cd(II), Mn(II) and Cr(III) in Fly Ash Based Geopolymers. *Constr. Build. Mater.* **2018**, *160*, 818–827. [CrossRef]
44. Aghazadeh, M.; Golikand, A.N.; Ghaemi, M. Synthesis, Characterization, and Electrochemical Properties of Ultrafine β-$Ni(OH)_2$ Nanoparticles. *Int. J. Hydrogen Energy* **2011**, *36*, 8674–8679. [CrossRef]
45. Persson, I. Hydrated Metal Ions in Aqueous Solution: How Regular Are Their Structures? *Pure Appl. Chem.* **2010**, *82*, 1901–1917. [CrossRef]
46. Hong, M.; Yu, L.; Wang, Y.; Zhang, J.; Chen, Z.; Dong, L.; Zan, Q.; Li, R. Heavy Metal Adsorption with Zeolites: The Role of Hierarchical Pore Architecture. *Chem. Eng. J.* **2019**, *359*, 363–372. [CrossRef]
47. Sheng, G.; Sheng, J.; Yang, S.; Hu, J.; Wang, X. Behavior and Mechanism of Ni(II) Uptake on MnO_2 by a Combination of Macroscopic and EXAFS Investigation. *J. Radioanal. Nucl. Chem.* **2011**, *289*, 129–135. [CrossRef]
48. Zhang, C.; Liu, X.; Lu, X.; Meijer, E.J.; Wang, R. An Atomic-Scale Understanding of the Initial Stage of Nucleation of Heavy Metal Cations on Clay Edges. *Geochim. Cosmochim. Acta* **2019**, *248*, 161–171. [CrossRef]
49. Kumar Jha, V.; Kameshima, Y.; Nakajima, A.; Okada, K.; MacKenzie, K.J.D. Effect of Grinding and Heating on Ni^{2+} Uptake Properties of Waste Paper Sludge. *J. Environ. Manag.* **2006**, *80*, 363–371. [CrossRef]
50. Dinu, M.V.; Dragan, E.S. Evaluation of Cu^{2+}, Co^{2+} and Ni^{2+} Ions Removal from Aqueous Solution Using a Novel Chitosan/Clinoptilolite Composite: Kinetics and Isotherms. *Chem. Eng. J.* **2010**, *160*, 157–163. [CrossRef]
51. Panasenko, A.E.; Shichalin, O.O.; Yarusova, S.B.; Ivanets, A.I.; Belov, A.A.; Dran'kov, A.N.; Azon, S.A.; Fedorets, A.N.; Buravlev, I.Y.; Mayorov, V.Y.; et al. A Novel Approach for Rice Straw Agricultural Waste Utilization: Synthesis of Solid Aluminosilicate Matrices for Cesium Immobilization. *Nucl. Eng. Technol.* **2022**, *54*, 3250–3259. [CrossRef]
52. Isawi, H. Using Zeolite/Polyvinyl Alcohol/Sodium Alginate Nanocomposite Beads for Removal of Some Heavy Metals from Wastewater. *Arab. J. Chem.* **2020**, *13*, 5691–5716. [CrossRef]
53. Sprynskyy, M.; Buszewski, B.; Terzyk, A.P.; Namieśnik, J. Study of the Selection Mechanism of Heavy Metal (Pb2+, Cu2+, Ni2+, and Cd2+) Adsorption on Clinoptilolite. *J. Colloid Interface Sci.* **2006**, *304*, 21–28. [CrossRef] [PubMed]
54. Tan, X.; Chen, C.; Yu, S.; Wang, X. Sorption of Ni^{2+} on Na-Rectorite Studied by Batch and Spectroscopy Methods. *Appl. Geochem.* **2008**, *23*, 2767–2777. [CrossRef]
55. Zhang, X.; Qin, Y.; Zhang, G.; Zhao, Y.; Lv, C.; Liu, X.; Chen, L. Preparation of PVDF/Hyperbranched-Nano-Palygorskite Composite Membrane for Efficient Removal of Heavy Metal Ions. *Polymers* **2019**, *11*, 156. [CrossRef]
56. Akpomie, K.G.; Dawodu, F.A. Acid-Modified Montmorillonite for Sorption of Heavy Metals from Automobile Effluent. *Beni-Suef Univ. J. Basic Appl. Sci.* **2016**, *5*, 1–12. [CrossRef]
57. Sharifian, S.; Asasian-Kolur, N.; Najafi, H.; Haddadi, B.; Jordan, C.; Harasek, M. Reusable Granulated Silica Pillared Clay for Wastewater Treatment, Selective for Adsorption of Ni(II). *Clean. Eng. Technol.* **2023**, *14*, 100634. [CrossRef]
58. Pomazkina, O.I.; Filatova, E.G.; Lebedeva, O.V.; Pozhidaev, Y.N. Adsorption of Nickel (II) Ions by Aluminosilicates Modified by Poly-1-Vinyl Imidazole and Poly-4-Vinyl Pyridine. *Prot. Met. Phys. Chem. Surfaces* **2018**, *54*, 582–586. [CrossRef]
59. Inumaru, K. "Sponge Crystal": A Novel Class of Microporous Single Crystals Formed by Self-Assembly of Polyoxometalate $(NH_4)_3PW_{12}O_{40}$ Nanocrystallites. *Catal. Surv. Asia* **2006**, *10*, 151–160. [CrossRef]
60. Wang, H.; Wang, X.; Xu, Z.; Zhang, M. Synthetic Zeolite from Coal Bottom Ash and Its Application in Cadmium and Nickel Removal from Acidic Wastewater. *Desalin. Water Treat.* **2016**, *57*, 26089–26100. [CrossRef]
61. Belova, T.P. Adsorption of Heavy Metal Ions (Cu^{2+}, Ni^{2+}, Co^{2+} and Fe^{2+}) from Aqueous Solutions by Natural Zeolite. *Heliyon* **2019**, *5*, e02320. [CrossRef]